International Journal of Heat and Mass Transfer 184 (2022) 122264

Contents lists available at ScienceDirect

International Journal of Heat and Mass Transfer

journal homepage: www.elsevier.com/locate/hmt

Method of reconstructing two-dimensional velocity fields on the basis of temperature field values measured with a thermal imaging camera

Krzysztof Tesch[a], Michał Ryms[b,*], Witold M. Lewandowski[b]

[a] Faculty of Mechanical Engineering and Ship Technology, Institute of Energy, Gdańsk University of Technology, Narutowicza 11/12, Gdańsk 80-233, Poland
[b] Faculty of Chemistry, Department of Energy Conversion and Storage, Gdańsk University of Technology, Narutowicza 11/12, Gdańsk 80-233, Poland

ARTICLE INFO

Article history:
Received 18 August 2021
Revised 9 November 2021
Accepted 14 November 2021
Available online 25 November 2021

Keywords:
Temperature field detection
Infrared imaging
CFD
Numerical velocity field reconstruction
Free convection in air
Vertical isothermal plate

ABSTRACT

This paper describes a novel numerical reconstruction procedure (NRP) of the velocity field during natural convective heat transfer from a two-sided, isothermal, heated vertical plate based only on the known temperature field obtained, e.g. with a thermal imaging camera. It has been demonstrated that with a knowledge of temperature distributions, the NRP enables the reconstruction of velocity fields by solving the Navier-Stokes equation with an additional momentum source term that replaces the Fourier-Kirchhoff equation. This is because its role is played by the known temperature field, which is the equivalent of its solution.

Experimental tests were performed in the air on a symmetrically heated, double-sided, isothermal vertical plate with dimensions of $150 \times 75 \times 2.1$ mm. In this test we used a thermal imaging camera with a temperature field detector in the form of a mesh parallel to the gravity acceleration vector, perpendicular to the heating surface and adjacent to the plate in the middle of its width. It was demonstrated that with a temperature field in the form of a results matrix, such reconstruction was possible and that the results obtained were consistent with other experimental results reported elsewhere and with SNC.

Along with recreating the velocity field using a standard numerical calculation (SNC), the temperature distributions and velocity fields of the plate under consideration were carried out in parallel and then compared with thermal imaging camera temperature measurements (CTM) and a reconstructed velocity field (NRP).

1. Introduction

Heat transfer in free convection, especially in the laminar regime, requires experimental tests of a special accuracy. This is because of the small heating surfaces, small temperature differences gradients and minimal heating powers involved. Measurements of heating power no longer pose a problem as electric current and voltage meters are increasingly precise. The same applies to local temperature and velocity measurements as a result of the miniaturisation and high accuracy of measurement sensors.

Contemporary measuring techniques such as PIV (Particle Image Velocimetry) allow one to obtain the velocity field by recording with a CCD camera while illuminating the entire field of tracer points with a stereoscopic laser beam and then to perform computer analysis of the distance of movement of all points on two superimposed and time-shifted images [5,7,16,26,28,29]. With LDA (Laser Doppler Anemometry), small velocity vectors can also be accurately measured [1,2,16]. Non-invasive velocity fields can be measured by combining these two methods, for example, to obtain results of turbulence measurements in an unsteady, swirling environment [6], or by applying all methods generally referred to as VBTP (Visualisation by Tracer Particles) and their combinations [11,21,27]. There are also well known and often used classical and holographic interferometry able to provide instantaneous temperature measurement. In practice, however, these methods are expensive and complicated. Moreover, by using liquid crystals [25] or complex measuring stands [30], one can also simultaneously gain temperature fields in liquids. Temperature fields in air can also be measured in a slightly different way by using a thermal imaging camera with a mesh as a temperature detector, which itself does not emit radiation in this wavelength range [28]. The latter method seems simpler and cheaper and that is why we decided to test it in this work.

* Corresponding author.
E-mail address: michal.ryms@pg.edu.pl (M. Ryms).

https://doi.org/10.1016/j.ijheatmasstransfer.2021.122264

Nomenclature

b	logical variable
c_p	specific heat capacity
f	index number of planar surfaces S_f around a control volume V_P
$\mathbf{g}$, g	gravity acceleration vector, magnitude of $\mathbf{g}$
H	height
$\mathbf{i}$, $\mathbf{j}$	unit normal vectors
k	turbulence kinetic energy
p, p_k	pressure, kinematic pressure
P	centroid of a finite volume V_P
Pr, $\mathrm{Pr_t}$	Prandtl and turbulent Prandtl numbers
Q	heat transfer rate
$\mathbf{r}$	position vector
R^2	coefficient of determination
Ra	Rayleigh number
$\mathbf{S}_f$	surface normal vector pointing outward
S_P	implicit momentum source coefficient
$\mathbf{S}_u$	explicit momentum source
t	time
T, T_0	temperature, reference temperature
$\mathbf{u}$	velocity vector field
u_x, u_y	velocity components
$\lvert V_P \rvert$	control volume measure around a centroid P
x, y, z	Cartesian coordinates
α	thermal diffusivity
β	coefficient of volumetric expansion
δ	boundary layer thickness
μ	dynamic viscosity
ν	kinematic viscosity
ρ	density
ω	turbulence frequency (specific dissipation rate)
CTM	camera temperature measurements
DES	detached eddy simulation
DNS	direct numerical simulation
LES	large eddy simulation
NRP	numerical reconstruction procedure
SNC	standard numerical calculation
RAS	Reynolds-averaged simulation

Unfortunately, not all configurations of convective heat transfer domains, shapes of heating surfaces and other conditions, especially in devices and heat exchangers, permit simultaneous measurements of temperature and velocity fields. For such cases, we describe a novel method for the numerical reconstruction of the velocity field (NRP), which can be determined under given conditions, based on an experimentally produced temperature field. The only precondition is that these fields are conjugate to each other: this is fulfilled in the case of free convection. This paper describes the method and results of the numerical transformation of a known temperature field in a reconstructed velocity field. This problem was already addressed in [22], but only for one velocity component parallel to gravity and on the assumption that the second component was negligible. The method described here makes it possible to reconstruct both components of the velocity field. The NRP developed in this work is correct for the Prandtl number $\mathrm{Pr} \approx 1.0$ (e.g. for air).

A vertical isothermal plate was selected for testing the possibility of numerically reconstructing the velocity field based on a known temperature distribution in free convection. This is the most accurately examined case of convective heat transfer [4,8,10]. In addition, a variant of a symmetrically heated plate was chosen in order to provide symmetrical heat transfer on both sides without heat losses [23].

2. The method of reconstructing velocity fields

The method described in [22] involves converting the temperature field from a thermal imaging camera into a two-dimensional velocity field. Since the Navier-Stokes, Fourier-Kirchhoff and continuity equations are mutually coupled, one can formulate the hypothesis that knowledge of the temperature field value is theoretically synonymous with knowledge of the velocity field value, at least in a free convection problem.

2.1. Earlier approach

Assuming steady state conditions as well as constant values of all the thermophysical properties of a fluid except for density, i.e. the kinematic viscosity, thermal diffusivity and thermal expansion, one can simplify the Fourier-Kirchhoff equation thus:

$$u_x \frac{\partial T}{\partial x} + u_y \frac{\partial T}{\partial y} = \alpha \left(\frac{\partial^2 T}{\partial x^2} + \frac{\partial^2 T}{\partial y^2} \right). \tag{1}$$

The viscous dissipation term is neglected here, and the Boussinesq approximation is used to account for buoyancy. This implies that the change of density caused by the temperature differences affects only the body force; the effects of these variations on the other terms of the momentum equations are ignored. This means that the incompressible form of the momentum equation can be taken into consideration.

Furthermore, in the case of two-dimensional, free convective heat transfer from a vertical plate in air, the temperature field in the fluid is caused by the density difference, which in turn, due to buoyancy, creates a fluid velocity field. All these variables are coupled, so if the temperature field is known, the fluid velocity can be determined. This also means that the temperature and velocity fields in free convection in a steady state condition are the same and that one follows from the other [22]. In order to apply Eq. (1), it has to be assumed further that $u_x \approx 0$, which in turns follows from the boundary layer assumption $u_y \gg u_x$. The above discussion and simplifications lead to the following equation for the vertical velocity coefficient [22]:

$$u_y = \frac{\alpha \left(\frac{\partial^2 T}{\partial x^2} + \frac{\partial^2 T}{\partial y^2} \right)}{\frac{\partial T}{\partial y}}. \tag{2}$$

It can also be assumed that $\frac{\partial^2 T}{\partial y^2} \approx 0$. This is because $\frac{\partial^2 T}{\partial x^2} \gg \frac{\partial^2 T}{\partial y^2}$, which is typical for the thermal boundary layer. The results are consistent with our own experimental results and those obtained by other authors [24] as well as with some numerical solutions [22]. However, the range of their application covered only the region of developed flow on the plate. In the region where the boundary layer forms, i.e. from the leading edge, where $y = 0$ to approximately $y = \frac{1}{5}$ of its height, in which the simplifying condition $u_y \gg u_x$ was not met, the discrepancies of the solution obtained with the experimental data and the results of the numerical calculations precluded its practical use. Therefore, a new approach to reconstructing the velocity field has been developed which does not require the previous simplifications.

2.2. Numerical reconstruction procedure (NRP)

2.2.1. Description of the novel method

This new method does not require any additional assumptions typical for the boundary layer, such as $u_x \approx 0$ or $\frac{\partial^2 T}{\partial y^2} \approx 0$. With the new approach one uses only the temperature distribution determined, for example, by means of a thermal imaging camera. The

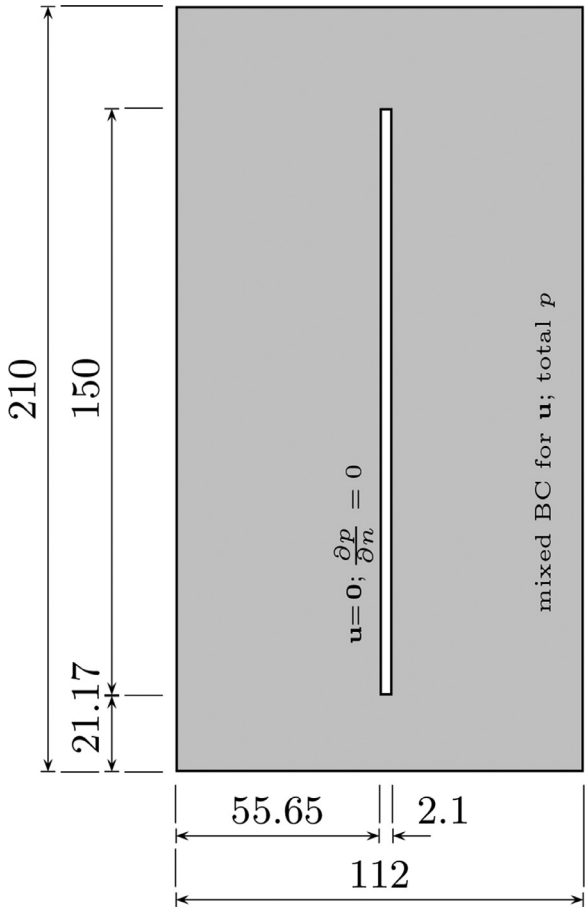

Fig. 1. NRP flow domain.

velocity field is then obtained by applying the numerical solution of the continuity equation together with the modified Navier-Stokes equation in the following form

$$\nabla \cdot \mathbf{u} = 0, \tag{3a}$$

$$\frac{\partial \mathbf{u}}{\partial t} + \nabla \cdot (\mathbf{u}\mathbf{u}) = \mathbf{S}_u - \nabla p_k + \nu \nabla^2 \mathbf{u}. \tag{3b}$$

Importantly, the NRP is valid for two-dimensional and free convective heat transfer problems, meaning that $\mathbf{u} = u_x\mathbf{i} + u_y\mathbf{j}$. The modified pressure p_k is defined as

$$p_k = \frac{p}{\rho_0} - \mathbf{g} \cdot \mathbf{r} \tag{4}$$

where the gravity acceleration vector $\mathbf{g} = -g\mathbf{j}$ is decomposed vertically according to Fig. 1 and $\mathbf{r} = y\mathbf{j}$ is the position vector.

Moreover, the proposed method does not require an additional Fourier-Kirchhoff equation to be solved, nor need any boundary conditions for temperature be set. This is because we use temperature distributions from an IR camera. In Eq. (3b), therefore, we add the additional term $\mathbf{S}_u$ related to the source of the momentum, which, of course, takes the form of an additional term related to the Boussinesq approximation

$$\mathbf{S}_u = -\beta(T - T_0)\mathbf{g}. \tag{5}$$

The influence of the temperature T on the velocity field occurs only through the momentum source term $\mathbf{S}_u$. In the above equation, β stands for the coefficient of volumetric expansion and T_0 is the known reference temperature. If our hypothesis is correct, we should obtain almost identical velocity fields from Eq. (3) supported by experimental results (e.g. CTM) and other typical solutions (e.g. SNC). This is how it should be and, as the calculations have shown, it is because the temperature and velocity are coupled for free convective heat transfer, i.e. the temperature differences are due to density variations which, due to buoyancy, create a velocity field.

2.2.2. Numerical procedure

To verify whether the NRP is correct, the existing software [19] was modified so that an additional source term calculated from equation (5) could be added to the centroid P of each finite volume V_P. The modified Navier-Stokes equation (3b) is discretised using the finite volume method [9,18] to give

$$\frac{\mathrm{d}\mathbf{u}_P}{\mathrm{d}t}|V_P| + \sum_f \mathbf{u}_f \mathbf{u}_f \cdot \mathbf{S}_f = \mathbf{S}_u|V_P| + S_P|V_P|\mathbf{u} - \sum_f p_{kf}\mathbf{S}_f + \nu \sum_f (\nabla \mathbf{u})_f \cdot \mathbf{S}_f. \tag{6}$$

Since the momentum source term (5) does not depend on $\mathbf{u}$, the implicit part of the linearised source term is zero $S_P|V_P|\mathbf{u} = \mathbf{0}$ and the whole momentum source term $\mathbf{S}_u$ is discretised explicitly as $\mathbf{S}_u|V_P|$, where $|V_P|$ is the control volume measure around the centroid P. Also, f is the index number of planar surfaces S_f around the control volume V_P.

The discretised convection term is interpolated by means of cell-centred values because the values of $\mathbf{u}_f$ are located at the face centroids. Bounded and limited linear interpolation (Total Variation Diminishing scheme) is used, as it is a blend of first- and second-order accurate with the blending coefficient 0.2 (0 stands for linear and 1 represents the strongest limiting). Furthermore, the discretised Laplacian terms involving surface normal gradients $(\nabla \mathbf{u})_f \cdot \mathbf{S}_f$ (evaluated at a cell face that connects two cells) utilise orthogonal schemes which are second-order accurate. Gradients such as $(\nabla \mathbf{u})_f$ and $(\nabla p_k)_f$, present in the Rhie-Chow interpolation method, involve Gaussian integration and linear interpolation. Finally, fluxes such as $\mathbf{u}_f \cdot \mathbf{S}_f$ also make use of linear interpolation. The governing equations are solved by means of the SIMPLE algorithm [3] and the pressure equation is solved using the generalised geometric-algebraic multi-grid solver with the diagonal-based incomplete Cholesky smoother. Smooth solvers with the Gauss-Seidel smoother are utilised for the velocity components. The underrelaxation factors are 0.3 for pressure and 0.7 for velocity.

The size of the computational mesh corresponds directly with the camera resolution and is 320×240. The domain dimensions are shown in Fig. 1. The impermeability and no adhesion condition, i.e. the no-slip condition, are specified on the plate accompanied by a zero-gradient condition for pressure. The least invasive boundary conditions are specified on the outer wall of the domain, i.e. mixed type velocity boundary conditions are applied. This means that for inflow, the velocity is obtained from the face normal component of the internal-cell value. For flow out of the domain, a zero-gradient condition is applied. Furthermore, the pressure p_k is calculated by a specification of the total pressure p_{k0}

$$p_k = p_{k0} - (1 - b)\tfrac{1}{2}\|\mathbf{u}\|^2 \tag{7}$$

where b is a logical variable. It becomes zero if the flux is positive or one otherwise.

It should be re-emphasised here that with such a system of equations and such boundary conditions, and without modifying the Navier-Stokes equation, we would obtain a trivial solution, i.e. a zero-velocity field, because the system of equations to be solved describes the incompressible flow without buoyancy. Only the modified Navier-Stokes equation containing an additional

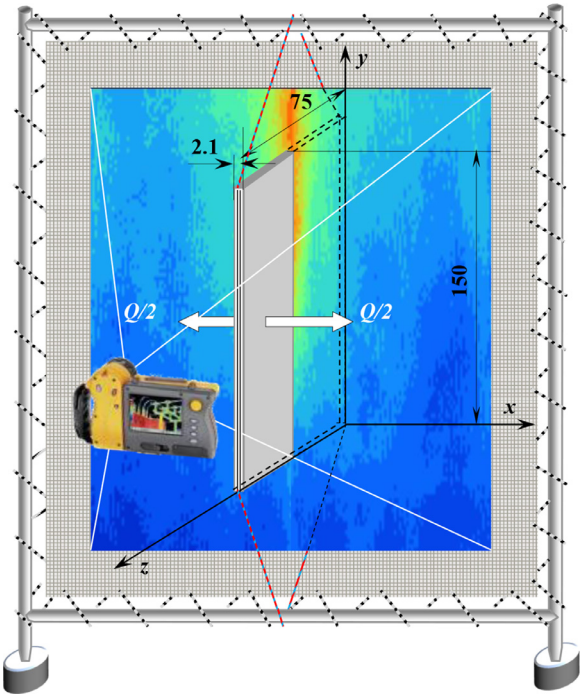

Fig. 2. Mutual positioning and fixing the elements of the experimental setup: an isothermal vertical plate, a mesh enabling detection of the temperature field in air and a thermal imaging camera [23].

temperature-dependent term (known by default from a thermal imaging camera) would permit the reconstruction of the velocity field on its basis.

The values of the parameters adopted for the calculations are $T_0 = 296.45\,\mathrm{K}$, $\beta = 0.003\,\mathrm{K}^{-1}$ and $\nu = 1.627 \cdot 10^{-5}\,\mathrm{m^2 s^{-1}}$. Results and comparisons are provided in Section 5.

3. Experimental studies

3.1. Experimental stand for determining the temperature field

In order to carry out convective heat transfer experiments in air from the vertical isothermal heating plate, an experimental stand was designed [23] consisting of a symmetrically heated isothermal plate, the heating system, regulating and measurement systems, a detection mesh and a thermal imaging camera. Fig. 2 shows the method for the mutual positioning of the mesh and cameras and the method of assembling them. The heating, measuring and regulatory systems that were shown and described in detail in [23] are omitted here.

The testing of temperature fields in air in a plane perpendicular to the isothermal heating plate determined using a thermal imaging camera and detection mesh are described in detail in [12] and [22]. A method of using these fields in the gradient method to determine heat fluxes in vertical channels and plate heat exchangers is given in [13] and [15]. In addition, a method of determining heat losses in construction elements, such as vertical walls, construction partitions and windows are described in [14].

We used a more sensitive and higher resolution E8 Thermal Imaging Camera (FLIR Systems Inc.) instead of a Fluke Ti35 camera to determine the temperature fields of the symmetrically, double-sided heated 150 mm plate. A E8 Thermal Imaging Camera with a temperature measurement accuracy of $\leq 0.1^{\circ}$C, as given in the device specification, was used for recording the temperature field. On this basis, it was assumed that the temperature measured with the IR camera was accurate to $\pm 0.1^{\circ}$C, but for the temperature differences the camera permits an accuracy of ± 0.01 K to be specified.

3.2. Experimental research

Experimental testing of free convection from the isothermal vertical plate in air for detecting temperature fields using a thermal imaging camera and mesh relies on a supply of heating power to a steady state condition in which the mesh has the same temperature as the surrounding convective stream of heated air. Cotton mesh fibres, of low thermal conductivity, counteracted the equalisation of their temperature on the surface of the mesh. These fibres were only heated by conductive heat transfer from the surrounding air, and the thermal inertia of the mesh fibres caused averaging and expiration of local fluctuations of the surrounding air temperature. Our results [23] indicate that scattered radiation, which reaches the mesh fibres from a perpendicular plate, distorts the measurements of temperature fields in a negligible degree. Moreover, it did not reach the mesh indirectly from the air, because without adsorbing the energy of this wave length, the air does not emit it either. The influence of radiation from this plate on the temperature field on the grid was analysed by measuring the constant $C = \mathrm{Nu}/\mathrm{Ra}^{1/4}$ using the balance method. In air this was $C = 1.220$, in water (without radiation) $C = 0.536$, and with the gradient method using the mesh $C = 0.614$ ($C = 0.796$ for $T_w = 303.15$ K, $C = 0.579$ for $T_w = 323.15$ K and $C = 0.534$ for $T_w = 343.15$ K) [23]. This analysis showed an overall discrepancy of 14.5% in the results obtained for convection with and without the radiation component. Because the discrepancy is also influenced by other factors, e.g. differences in the balance and gradient measurement methods and their accuracy, the error for temperature indications on the mesh will be even smaller.

The experiments were carried out at the following heating plate temperatures: $T_w =$ 300.35, 305.05, 312.85, 317.05, 320.65, 323.85, 328.15, 330.45, 333.25, 335.45, 339.35, 342.75 K at the free stream temperature $T_\infty = 295.65$–296.95 K, with these thermal conditions corresponding to the range of the Rayleigh number $\mathrm{Ra} = 10^6$–10^7 [23]. One of the many temperature distributions was chosen for the numerical reconstruction of the velocity field for $T_w = 328$ K, $T_\infty = 296$ K, $\Delta T = 32$ K, $T_{av} = 312$ K and is presented graphically in Fig. 3.

4. Numerical simulations of the test experiment

In order to compare the velocity field obtained by means of the method discussed in paragraph 2.2, a standard numerical calculation (SNC) of the experimental data (T_w, T_∞) was carried out in the domain with dimensions shown in Fig. 4. In addition to comparing the velocity fields with the NRP, it was also possible to compare the temperature distributions with the CTM. The calculation model was adopted in the most general way, which does not take the Boussinesq approximation into account. This permits an additional assessment of the suitability of the proposed method of determining the velocity fields based on temperature fields (NRP). Turbulent compressible flow was taken into account, which is described by the continuity equation, the Reynolds equation, the equation of energy in the form of sensible enthalpy (viscous dissipation term included) along with a thermal equation of state. The turbulence modelling involved a Reynolds Averaged Simulation together with turbulence closure based on linear eddy viscosity, i.e. the Boussinesq hypothesis. The two-equation $k - \omega$ SST [17] was also taken into account. The RAS approach is generally necessary as it suppresses velocity fluctuations, just as when a measuring mesh is used. As the accuracy of the method increases (DES/LES and DNS approaches), the complexity of the flow itself also grows, which is

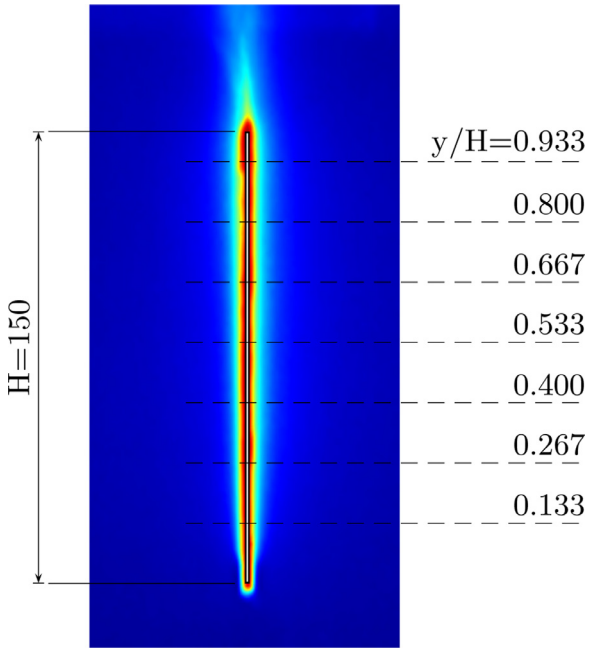

Fig. 3. Temperature fields visualised on the basis of the results matrix from the thermal imaging camera for the case $H = 150$ mm, $s = 2.1$ mm, $T_w = 328$ K, $T_\infty = 296$ K, $\Delta T = 32$ K, $T_{av} = 312$ K, $\mathrm{Ra} = 8.53 \cdot 10^6$ [23].

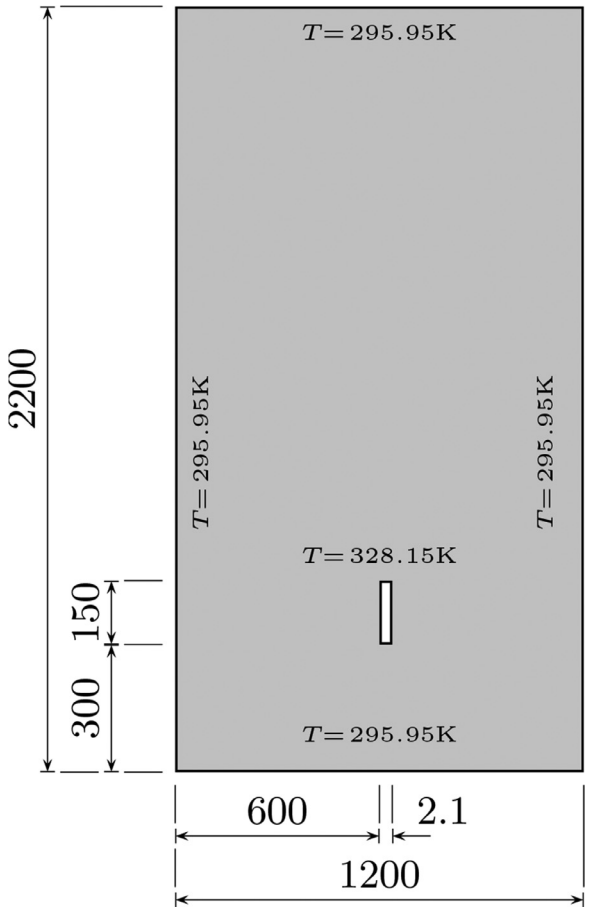

Fig. 4. SNC flow domain.

Table 1
SNC mesh statistics.

	Small	Medium	Fine
Nodes	590 430	1 324 698	**2 495 416**
Faces	1 177 299	2 644 056	**4 981 184**
Faces per cell		6	
Total volumes	294 028	660 569	**1 244 492**

manifested by the appearance of ever smaller vortices and fluctuations in the solutions. Fluctuations are present in the flow, but the measuring grid only show the average values that correspond to the RAS method.

The discretisation procedure follows the same logic as in the previous case. Convection terms, including velocity, enthalpy, kinetic energy as well as the turbulent quantities k and ω, are interpolated by means of bounded and limited linear interpolation schemes with blending coefficient of 0.2. Also, all the discretised Laplacian terms utilise orthogonal schemes. All gradients involve Gaussian integration and linear interpolation. Lastly, all fluxes utilise linear interpolation. The same line of reasoning applies to the method of solving governing equations, i.e. the SIMPLE algorithm. The pressure equation is solved by means of the generalised geometric-algebraic multi-grid solver with the combined diagonal-based incomplete Cholesky (DIC) and Gauss-Seidel smoother in which DIC smoothing is followed by Gauss-Seidel. The stabilised preconditioned bi-conjugate gradient solvers with the simplified diagonal-based incomplete LU (Lower-Upper) preconditioner are utilised for the velocity components, enthalpy and turbulence quantities. Underrelaxation factors are 0.7 for pressure, 0.3 for velocity and enthalpy and 0.7 for turbulence quantities k and ω.

The no-slip condition is specified everywhere accompanied by a fixed temperature 295.95 K, except for the surface of the plate, where the temperature is 328.15 K. Also, the pressure gradient is calculated such that the flux on the boundary follows the velocity boundary condition. This means that the pressure gradient comes from the same equation as the discretised Navier-Stokes (Reynolds) equation interpolated next to the boundary face. Then, in order to make sure that the flow near the walls is properly resolved, thin layers around the physical walls are generated in such a way that the maximum y^+ values are lower than 1 for the plate walls. A scalable wall function is also applied in order to ensure stability. Turbulent quantities are set according to the low turbulence intensity, and the turbulent Prandtl number is $\mathrm{Pr_t} = 0.85$. Finally, the constant values of other parameters adopted for calculations are $c_p = 1004\,\mathrm{J\,kg^{-1}K^{-1}}$, $\mathrm{Pr} = 0.705$ and $\mu = 1.831 \cdot 10^{-5}\,\mathrm{kg\,m^{-1}s^{-1}}$.

The two-dimensional computational mesh consists of hexahedral elements and is classified as Cartesian. The detailed mesh statistics for individual cases are shown in Table 1. Three cases were considered: small, medium and fine. The influence of the mesh on the velocity distribution is shown in Fig. 5 (a). The plot shows u_y velocity component distributions on a $y/H = 0.8$ line relative to the lower surface of the plate (see Fig. 3). There is virtually no difference between the medium and fine mesh sizes. Fig. 5 (b) shows the temperature distributions at the same height. No visual differences are perceptible. Therefore, it was decided to choose a fine mesh because the difference between the medium and fine meshes is negligible, except for the smoothness of the velocity distribution for the latter. The results of SNC and comparisons with NRP and CTM are given in Section 5.

5. Results

The u_x and u_y velocity distributions, obtained using the NRP and SNC methods, for different y/H height ratios of the vertical

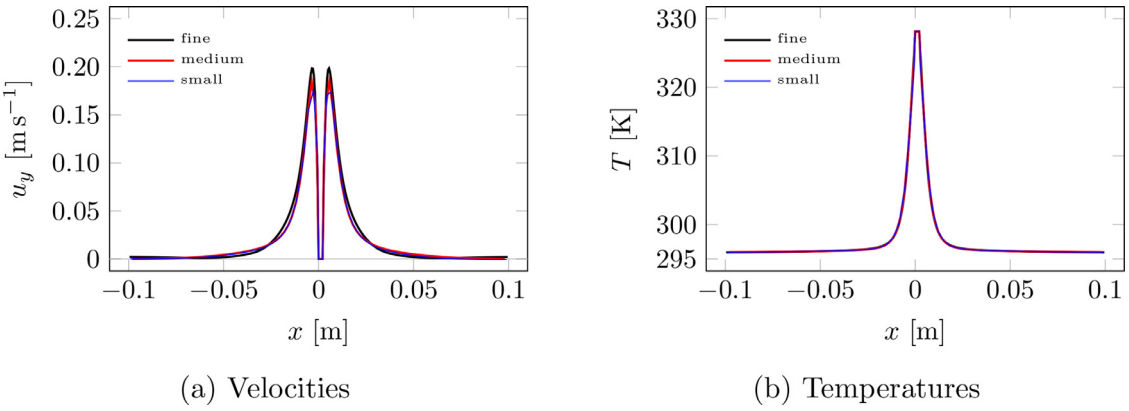

Fig. 5. SNC mesh convergence $y/H = 0.8$.

Table 2
Coefficient of determination R^2.

h/H	$R^2(T)$	$R^2(u_x)$	$R^2(u_y)$
0.133	0.841	0.930	0.828
0.267	0.858	0.920	0.884
0.400	0.875	0.928	0.899
0.533	0.883	0.944	0.904
0.667	0.902	0.922	0.921
0.800	0.943	0.911	0.939
0.933	0.905	0.994	0.950

isothermal plate, are compared in Fig. 8 with the superimposed theoretical (similarity) solutions [20] as a reference. Evidently, the u_y components coincide very well in the distance along the x axis from the plate to the extreme velocity values. The same holds for the u_x velocity components. As the distance from the plate increases, so do the differences between the various methods. Nevertheless, the qualitative compatibility of the two methods is evident. The temperature distributions for the SNC and CTM methods are shown in Fig. 9. As in the case of Fig. 8, the qualitative compatibility of both methods is clearly visible. The differences in the velocity distributions result from the finite resolution of the camera and the necessity to determine the boundary conditions for the NRP method at a short distance from the plate, which is approximately equal to the thickness of the hydrodynamic boundary layer δ.

The quantitative comparison of individual methods is shown in Table 2 using the coefficient of determination R^2. In the worst case, this coefficient reaches the value of 0.841 for the comparison of the temperatures obtained from the experiment (CTM) and calculated using the SNC method. For the u_x velocity component, the minimum R^2 value is 0.911 while for the u_y component we have 0.828. However, the differences also result from the method of calculating R^2 which, among other things, involves adding up the individual components. Finally, the results can only be regarded as a satisfactory qualitative verification.

A further comparison of the two methods is possible using the heat transfer rate Q balances in a cuboidal control volume around the vertical plate according to the following equation

$$Q_o = \bar{\rho}\,\delta\,H\,\bar{u}_{yo}\,c_p\left(\bar{T}_o - \bar{T}_i\right). \tag{8}$$

A graphic illustration of the balance together with the u_y and T values calculated in two ways (SNC and NRP) and the plate heating power measured directly during the experimental tests are shown in Fig. 6. The heat transfer rate supplied from the plate to the air

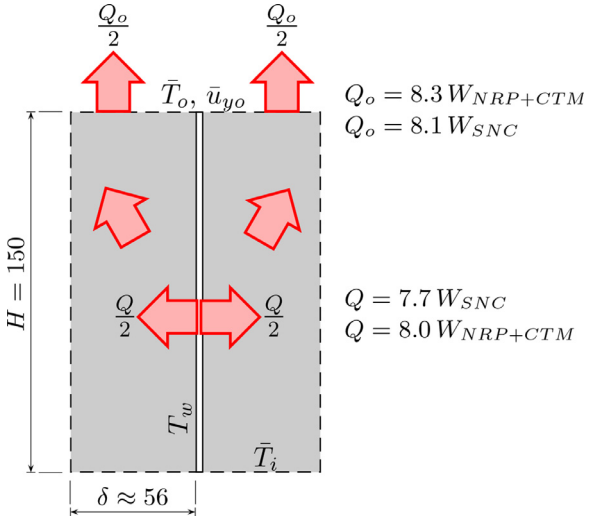

Fig. 6. Heat transfer rates from the plate.

Table 3
Averaged values.

	Q [W]	Q_o [W]	$\bar{T}_0$ [K]	$\bar{T}_i$ [K]	$\bar{u}_{yo}$ [m s^{-1}]
SNC	7.7	8.1	299.3	297.2	0.046
NRP+CTM	8.0	8.3	297.7	296.4	0.066

is denoted by Q and the withdrawn heat transfer from the control volume via the upper surface by Q_o, while the average temperatures in the lower and upper parts of the area are respectively labelled $\bar{T}_i$ and $\bar{T}_0$. The vertical component of the averaged velocity $\bar{u}_{yo}$ in the upper part of the area is needed in order to calculate the mass flow rate.

Table 3 presents the result of the quantitative verification of the correctness of the velocity reconstruction using the NRP method, carried out by the balance method. The heat transfer rates in the upper part of the area are similar for the individual methods, i.e. $Q = 8.1$ W for the SNC method and 8.3 W for the NRP+CTM methods, where the temperature fields come from the experimental CTM measurements and the velocities from the NRP method. Then, the heat transfer rate generated on the plate is $Q = 8.0$ W according to the experimental data from the direct measurement, and $Q = 7.7$ W according to the SNC method. It can be seen that the

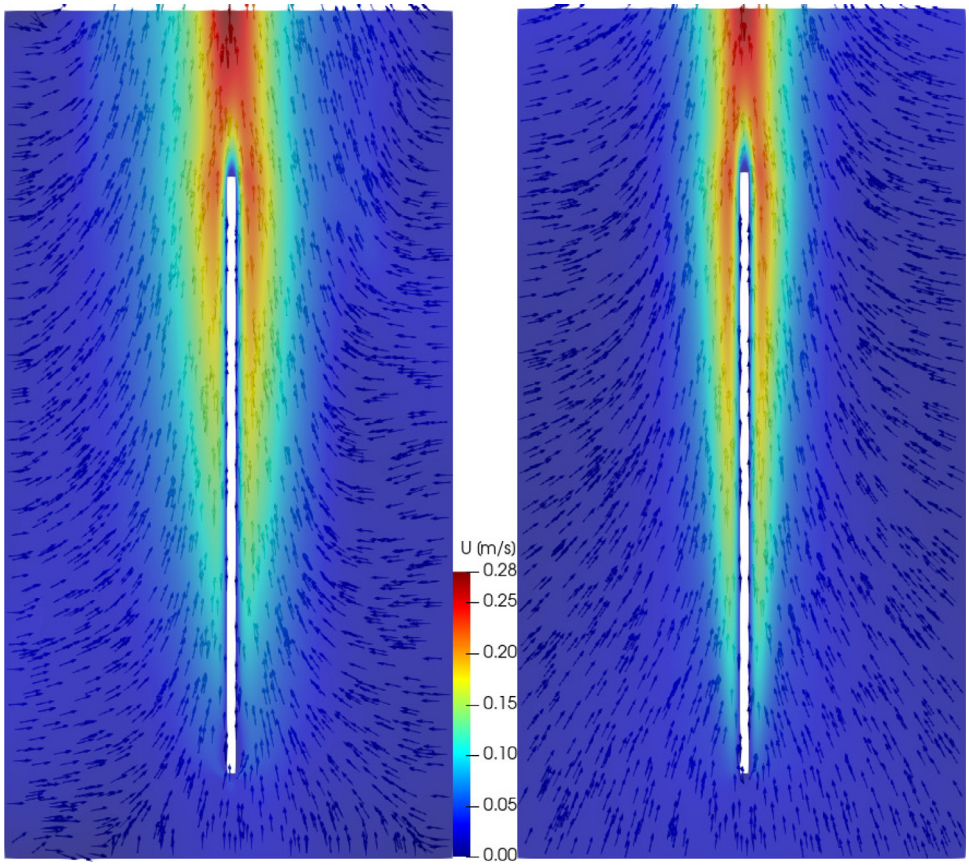

Fig. 7. Velocity field visualisation: NRP (left) vs. SNC (right).

heat transfer rate calculated according to Eq. (8) is slightly overestimated. As the difference between the Q_o for each method is only 2.4%, the verification of the NRP method can be considered successful.

Figure 7 shows the visualisation of velocity fields for NRP and SNC methods in the form of a velocity vector magnitude with a superimposed vector field. All vectors have an identical length and differ in colour that corresponds directly to the magnitude. Both solutions are very similar qualitatively. Noteworthy is the slight impact of boundary conditions for the NRP method, which is visible on the left and right wall.

6. Summary and conclusions

The study described in this paper shows that it is possible to numerically reconstruct the velocity field solely on the basis of a known temperature field, measured experimentally, in our case using a thermal imaging camera with a mesh detector. This is confirmed by solving the Navier-Stokes equations with an additional momentum source term by means of the finite volume method. The proposed procedure does not require assumptions such as $u_x \approx 0$ or $\frac{\partial^2 T}{\partial y^2} \approx 0$, applied in the previous version of the method [22]. Nevertheless, the full velocity fields, i.e. u_x and u_y, were resolved throughout the range of natural convective around the isothermal, two-sided, heated vertical plate. The accuracy of the results obtained by means of NRP and SNC is evident, but as a result of summing all u_x and u_y values, the coefficient of determination R^2 takes values from 0.828 upwards, so the verification can only be regarded as qualitatively satisfactory.

The quantitative verification of the method carried out on the basis of the balance of two heat transfer rates Q gives a better accuracy. The former heat transfer rate is generated from the plate to the air, while the latter is released into the air. Since the first of these heat rates was based on the measured temperature field (CTM) and the other independently on the basis of the reconstructed velocity field (NRP), their accuracy at 2.4% is already an obvious quantitative confirmation of the correctness of the proposed method (NRP).

The accuracy of the reconstructed velocity fields, according to the proposed method, depends on the accuracy of the measurement of temperature fields and can be improved by increasing the resolution of the thermal imaging camera, because its resolution corresponds directly to the exact size of the computational mesh used to reconstruct the velocity field.

Having demonstrated the compliance of the NRP with the results of experimental and numerical tests, the authors indicate some of its possible applications, e.g. by researchers who use liquid crystals (for example [25]) that can only measure temperatures or engineers who measure heat losses from real objects (building façades, boiler walls, devices, etc.) where it seems easier to use our method with an IR camera than to determine the temperature field with thermocouples and velocity sensors (e.g. DISA hot wire anemometer). Moreover, the NRP method can be used to automatically reconstruct free convective velocity fields in air using thermal imaging cameras. Theoretically, the method can also be used to study three-dimensional cases, but then the mesh will have to be moved along the z axis. Such a displacement will disturb the flow, however, and will prolong the measurement time by the periods required to restore thermodynamic equilibrium each time the mesh has been shifted. Finally, the method developed in this work is correct for $\mathrm{Pr} \approx 1.0$, i.e. for air. For other liquids $\mathrm{Pr} \neq 1.0$, e.g. water, additional verification of the NRP is required.

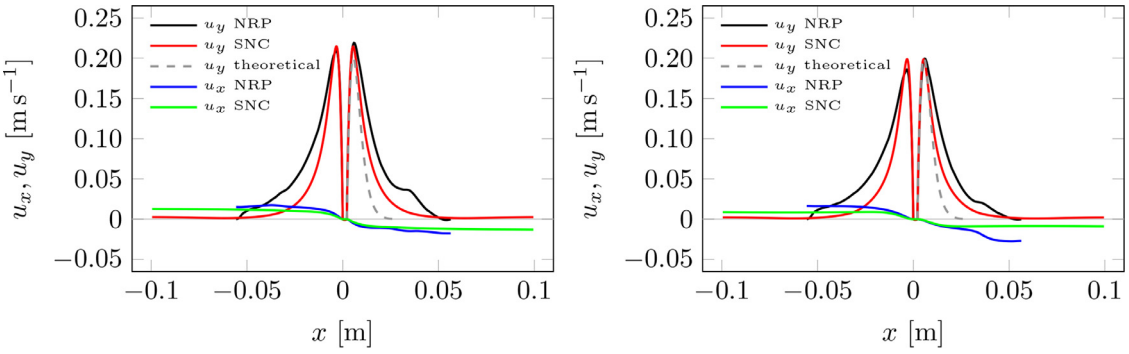

(a) $y/H = 0.933$ (b) $y/H = 0.800$

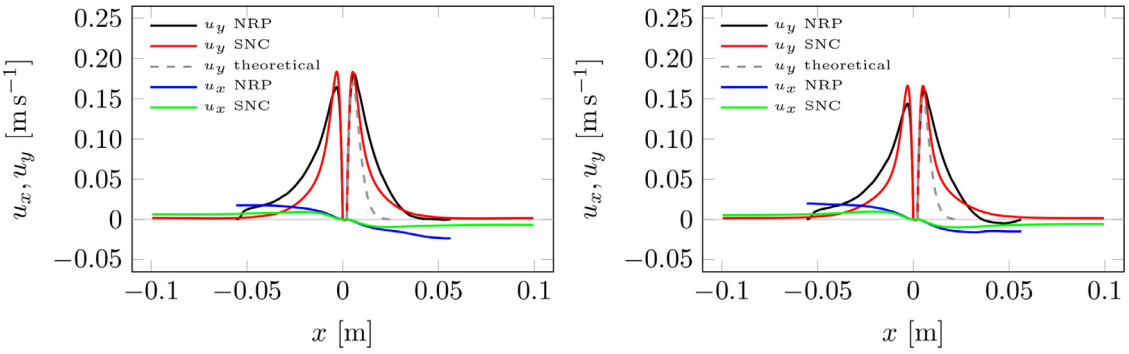

(c) $y/H = 0.667$ (d) $y/H = 0.533$

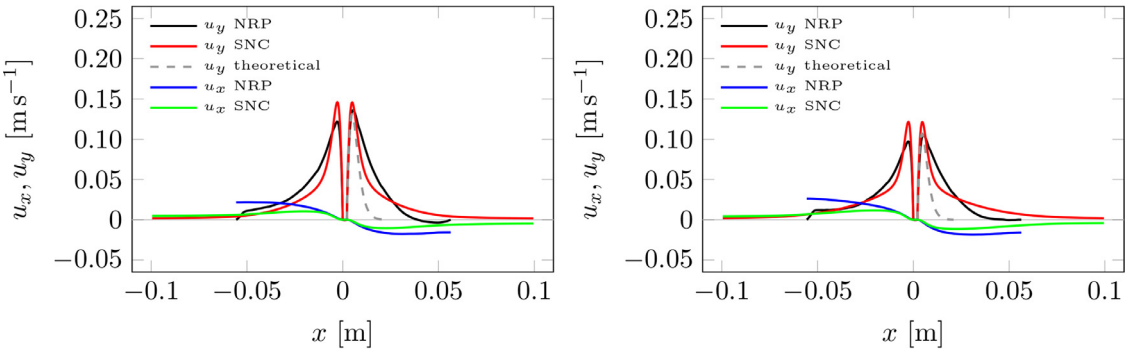

(e) $y/H = 0.400$ (f) $y/H = 0.267$

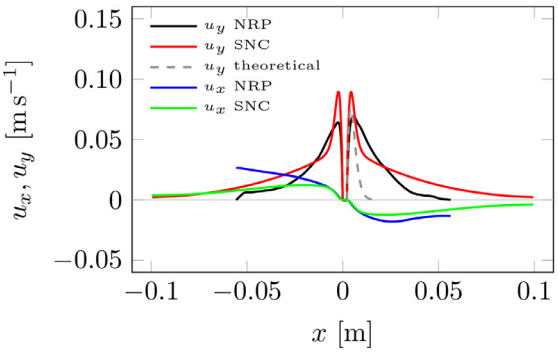

(g) $y/H = 0.133$

Fig. 8. Velocity distributions: NRP vs. SNC.

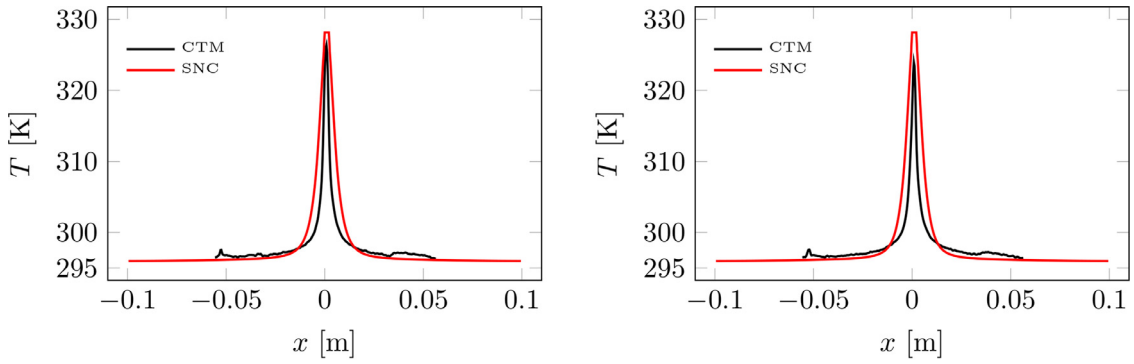

(a) $y/H = 0.933$

(b) $y/H = 0.800$

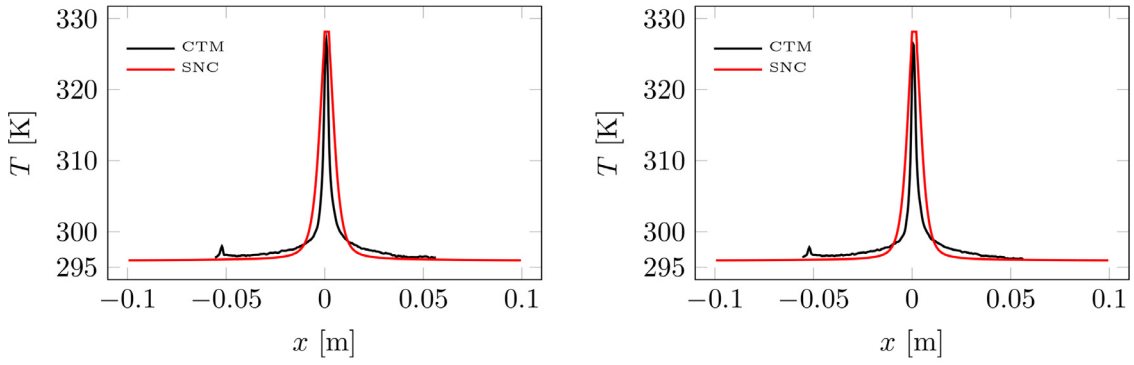

(c) $y/H = 0.667$

(d) $y/H = 0.533$

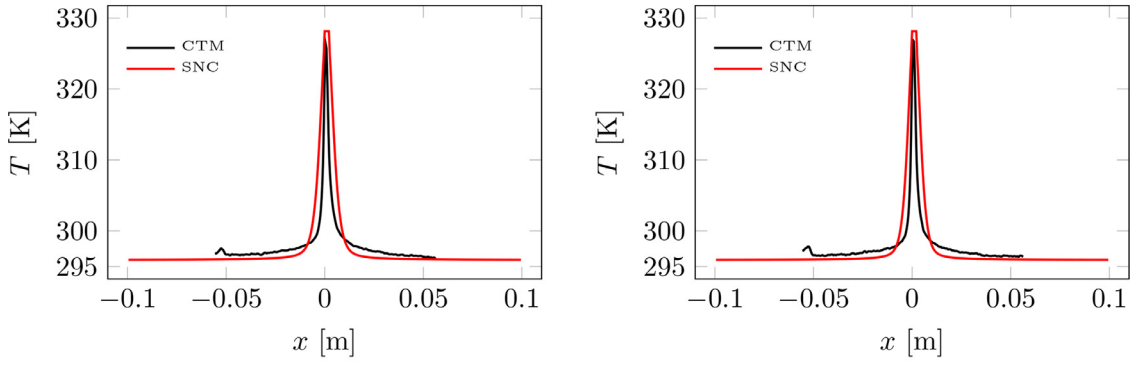

(e) $hy/H = 0.400$

(f) $y/H = 0.267$

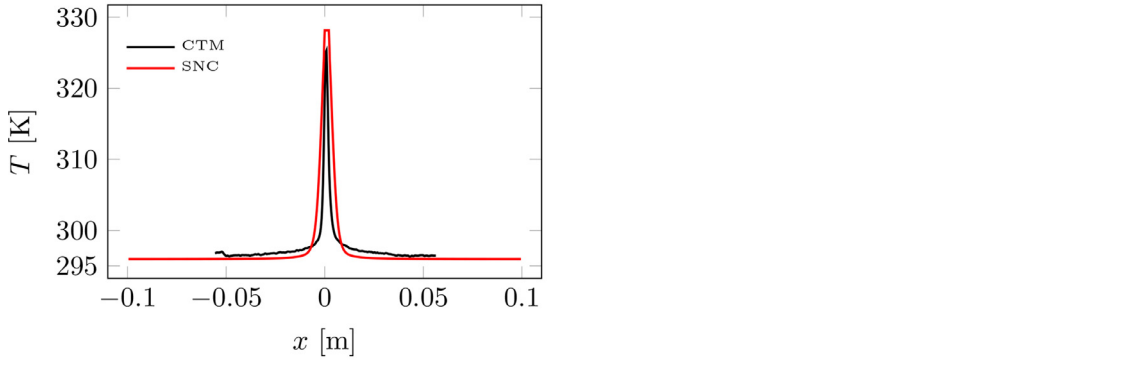

(g) $y/H = 0.133$

Fig. 9. Temperature distributions: CTM vs. SNC.

Declaration of Competing Interest

We wish to confirm that there are no known conflicts of interest associated with this publication and there has been no significant financial support for this work that could have influenced its outcome.

We confirm that the manuscript has been read and approved by all named authors and that there are no other persons who satisfied the criteria for authorship but are not listed. We further confirm that the order of authors listed in the manuscript has been approved by all of us.

We confirm that we have given due consideration to the protection of intellectual property associated with this work and that there are no impediments to publication, including the timing of publication, with respect to intellectual property. In so doing we confirm that we have followed the regulations of our institutions concerning intellectual property.

We understand that the Corresponding Author is the sole contact for the Editorial process (including Editorial Manager and direct communications with the office). He is responsible for communicating with the other authors about progress, submissions of revisions and final approval of proofs. We confirm that we have provided a current, correct email address which is accessible by the Corresponding Author and which has been configured to accept email from International Journal of Heat and Mass Transfer: michal.ryms@pg.edu.pl

CRediT authorship contribution statement

Krzysztof Tesch: Conceptualization, Formal analysis, Validation, Writing – original draft, Writing – review & editing. **Michał Ryms:** Conceptualization, Methodology, Data curation, Investigation, Writing – original draft, Writing – review & editing. **Witold M. Lewandowski:** Conceptualization, Writing – review & editing, Visualization, Validation, Supervision.

References

[1] L.R. Cairnie, A.J. Harrison, Natural convection adjacent to a vertical isothermal hot plate with a high surface-to-ambient temperature difference, Int. J. Heat Mass Transfer 25 (1982) 925–934, doi:10.1016/0017-9310(82)90068-0.

[2] S. Caliskan, S. Baskaya, Velocity field and turbulence effects on heat transfer characteristics from surfaces with v-shaped ribs, Int. J. Heat Mass Transfer 55 (2012) 6260–6277, doi:10.1016/j.ijheatmasstransfer.2012.06.056.

[3] L.S. Caretto, A.D. Gosman, S.V. Patankar, D.B. Spalding, Two calculation procedures for steady, three-dimensional flows with recirculation, in: H. Cabannes, R. Temam (Eds.), Proceedings of the Third International Conference on Numerical Methods in Fluid Mechanics. Lecture Notes in Physics 19, Springer, Berlin, Heidelberg, 1973.

[4] S.W. Churchill, H.H.S. Chu, Correlating equations for laminar and turbulent free convection from a vertical plate, Int. J. Heat Mass Transfer 18 (11) (1975) 1323–1329, doi:10.1016/0017-9310(75)90243-4.

[5] S. Grafsronningen, A. Jensen, B.A.P. Reif, PIV Investigation of buoyant plume from natural convection heat transfer above a horizontal heated cylinder, Int. J. Heat Mass Transfer 54 (2011) 4975–4987, doi:10.1016/j.ijheatmasstransfer.2011.07.011.

[6] N. Grosjean, L. Graftieaux, M. Michard, W. Hubner, C. Tropea, J. Volkert, Combining LDA and PIV for turbulence measurements in unsteady swirling, Meas. Sci. Technol. 8 (1997), doi:10.1088/0957-0233/8/12/015.

[7] Y. Hattori, T. Tsuji, Y. Nagano, N. Tanaka, Effects of free stream on turbulent combined-convection boundary layer along a vertical heated plate, Int. J. Heat Fluid Flow 22 (2001) 315–322, doi:10.1016/S0142-727X(01)00094-7.

[8] Y. Jaluria, Natural Convection Heat and Mass Transfer, Pergamon Press, Oxford, 1980.

[9] H. Jasak, Error Analysis and Estimation for the Finite Volume Method with Applications to Fluid Flows, PhD Thesis, 1996.

[10] L.M. Jiji, Heat Convection, Springer-Verlag, Berlin Heidelberg, 2009.

[11] D. Kim, D. Kim, M. Kim, J. Lee, I. Jung, K. Roh, K.C. Kim, Velocity field measurement on natural convection inside an automotive headlamp using time-resolved stereoscopic particle image velocimetry, Int. J. Heat Fluid Flow 77 (2019) 19–30, doi:10.1016/j.ijheatfluidflow.2019.03.004.

[12] W.M. Lewandowski, M. Ryms, H. Denda, E. Klugmann-Radziemska, Possibility of thermal imaging use in studies of natural convection heat transfer on the example of an isothermal vertical plate, Int. J. Heat Mass Transfer 78 (2014) 1232–1242, doi:10.1016/j.ijheatmasstransfer.2014.07.024.

[13] W.M. Lewandowski, M. Ryms, H. Denda, Infrared techniques for natural convection investigations in channels between two vertical, parallel, isothermal and symmetrically heated plates, Int. J. Heat Mass Transfer 114 (2017) 958–969, doi:10.1016/j.ijheatmasstransfer.2017.06.120.

[14] W.M. Lewandowski, M. Ryms, H. Denda, Quantitative study of free convective heat losses from thermodynamic partitions using thermal imaging, Energy Build 167 (2018) 370–383, doi:10.1016/j.enbuild.2017.12.047.

[15] W.M. Lewandowski, M. Ryms, H. Denda, Natural convection in symmetrically heated vertical channels, Int. J. Therm. Sci. 134 (2018) 530–540, doi:10.1016/j.ijthermalsci.2018.08.036.

[16] J.A. McWilliams, Review of airflow measurement techniques, LBNL Report Number, LBNL-49747 (2002) 1–113.

[17] F.R. Menter, Two-equations eddy-viscosity turbulence models for engineering applications, AIAA Journal 32 (8) (1994) 1598–1605, doi:10.2514/3.12149.

[18] F. Moukalled, L. Mangani, M. Darwish, The Finite Volume Method in Computational Fluid Dynamics, Springer, 2016.

[19] OpenFOAM, https://www.openfoam.com.

[20] S. Ostrach, An analysis of laminar free-convection flow and heat transfer about a flat plate parallel to the direction of the generating body force, Technical Note 2635, NACA, 1952.

[21] H. Park, J. Park, S.Y. Jung, Measurements of velocity and temperature fields in natural convective flows, Int. J. Heat Mass Transfer 139 (2019) 293–302, doi:10.1016/j.ijheatmasstransfer.2019.05.022.

[22] M. Ryms, K. Tesch, W.M. Lewandowski, The use of thermal imaging camera to estimate velocity proiles based on temperature distribution in a free convection boundary layer, Int. J. Heat Mass Transfer 165 (2021) 120686, doi:10.1016/j.ijheatmasstransfer.2020.120686.

[23] M. Ryms, W.M. Lewandowski, Evaluating the influence of radiative heat flux on convective heat transfer from a vertical plate in air using an improved heating plate, Int. J. Heat Mass Transfer 173 (2021) 121232, doi:10.1016/j.ijheatmasstransfer.2021.121232.

[24] E. Schmidt, W. Beckmann, Das temperatur- und geschwindigkeitsfeld vor einer wärme abgebenden senkrechten platte bei natürlicher konvektion, Technische Mechanik und Thermodynamik 1 (1930) 391–406, doi:10.1007/BF02640222.

[25] J. Stasiek, T.A. Kowalewski, The use of thermochromic liquid crystals in heat transfer research, Proceedings of SPIE 4759 (2002) 374–383.

[26] R.S. Volkov, P.A. Strizhak, Research of temperature fields and convection velocities in evaporating water droplets using planar laser-induced fluorescence and particle image velocimetry, Exp. Therm Fluid Sci. 97 (2018) 392–407, doi:10.1016/j.expthermflusci.2018.05.007.

[27] R.S. Volkov, P.A. Strizhak, Using planar laser induced fluorescence and micro particle image velocimetry to study the heating of a droplet with different tracers and schemes of attaching it on a holder, Int. J. Therm. Sci. 159 (2021) 106603, doi:10.1016/j.ijthermalsci.2020.106603.

[28] C.E. Willert, M. Gharib, Digital particle image velocimetry, Exp Fluids 10 (1991) 181–193, doi:10.1007/BF00190388.

[29] T. Xue, S. Zhang, Investigation on heat transfer characteristics of falling liquid film by planar laser-induced fluorescence, Int. J. Heat Mass Transfer 126 (2018) 715–724, doi:10.1016/j.ijheatmasstransfer.2018.05.039.

[30] O.S. Bharti, A.K. Saha, M.K. Das, S. Bansal, Simultaneous measurement of velocity and temperature fields during natural convection in a water-filled cubical cavity, Exp. Therm Fluid Sci. 99 (2018) 272–286, doi:10.1016/j.expthermflusci.2018.07.039.